Laser Ultrasonics Inspection for Defect Evaluation on Train Wheel

Nicola Montinaro[1]*, Gabriella Epasto[2], Donatella Cerniglia[1], Eugenio Guglielmino[2]

[1] Dipartimento di Ingegneria, Università degli Studi di Palermo, Viale delle Scienze Edificio 8, 90128 Palermo, Italy.

[2] Dipartimento di Ingegneria, Università degli Studi di Messina, Contrada di Dio, Sant'Agata, 98166 Messina, Italy.

*corresponding author: nicola.montinaro@unipa.it

Keywords

Non-destructive testing; non-contact techniques; laser ultrasonic; train wheel inspection.

Abstract

Passengers' safety and in-service life of wheelset axles play an important role in railway vehicles. For this reason, periodic inspections are necessary. Among non-destructive techniques, ultrasonic ones are widely applied in this field. The main disadvantage of conventional ultrasonic techniques is that the overall inspection of wheels requires the train to be put out-of-service and disassembly each part, which is time-consuming and expensive.

In this paper, a non-conventional non-contact laser ultrasonic inspection for train wheels is proposed. The proposed method uses a laser interferometer to receive the ultrasonic wave without contact. The receiving system allows choosing the distance between the surface to be inspected and the interferometer, overcoming any encumbrance issue. The experimental investigation is carried

out on standard-reproduced defects in order to evaluate the reliability and the accuracy of the technique and to verify its applicability for railway components, as wheels, which have a complex geometry. The experimental setup consists of a pulsed laser for the ultrasonic wave generation. The receiving unit combines a continuous-wave laser and an interferometer in order to acquire the surface out-of-plane displacements. Surface and internal standard defects are detected by collecting all the A-scans in a B-scan map. The results are promising for the application of the laser technique to detect both surface and internal defects on in-service components.

1. Introduction

In the railway field, passengers' safety and service life of axles and wheels are a fundamental topic. Railway wheels have to withstand severe static and dynamic loads deriving from their operating conditions. They are subjected mainly to cyclic thermal load, residual stresses and to rolling contact fatigue [1,2], that can lead to the failure of the wheels, even though they are designed to infinite fatigue life (about 30 years or more) [3]. Considering that fatigue stresses can induce the initiation of cracks, short-time-spaced non-destructive inspections aim at ensuring that such cracks are below the critical size or even absent [4].

It is well known that fatigue cracks initiate on the component surface; even though over 10^7 cycles, in steel, fatigue cracks can nucleate also inside the component [5]. For this reason, the detection of surface cracks and defects in some cases cannot be sufficient for safety reasons; thus, volumetric non-destructive techniques are recommended.

Non-destructive evaluation is widely employed in the railway field. Some recent studies concern with the application of non-conventional techniques for defect and crack detection in rail [6,7] and axle [8–10]. For wheel inspection, innovative techniques consist in the application of sensor array to monitor anomalies. Filograno et al. [11] applied FBG sensing systems to detect out-of-roundness in train wheels tested at the maximum in-service speed. Wheel impact load detectors were studied by Stratman et al. [12] to provide a quantitative decision method for putting out-of-service defective

wheels.

Nowadays, conventional methods are generally applied, such as eddy current testing and magnetic particle testing [4]. Some researches consider the importance of non-destructive evaluation of rail wheels [13–17] as they can be involved in fatigue failure, with catastrophic consequences [18].

Among non-destructive techniques, conventional ultrasonic ones are the most common, for instance to inspect the rolling surfaces of the wheels [19] or for defect evaluation using phased array technology [20]. The main disadvantage of conventional techniques is that the overall inspection of the wheelset axles requires the train to be put out-of-service and the disassembly of each element, which may be time-consuming and expensive. Moreover, a preparation of the surfaces and a coupling media (water or gel) is always recommended in order to ensure a contact between the probe and the object to be inspected. Such practical problems, especially for on-site inspections, can be overcome by non-contact ultrasonic techniques, which use a pulsed laser for the generation of the ultrasonic waves and different waves' receiving devices.

Non-contact laser generation of ultrasound in solids is an effective method to generate guided mode acoustic signals, such as Rayleigh and Lamb waves [21,22]. This method offers the advantage of non-contact and remote (distant from the specimen) ultrasonic testing, enabling railroad-related and other industrial inspection applications that are not possible with conventional techniques. In addition, just one laser source and one receiving device are enough for defect detection in the wheel; whereas, with phased array technique, a number of elements is required [20]. The main cons of the laser-laser UT, in respect to the phased array, is the more time required to inspect the same area coverage, due to the punctual focalizations of the lasers, and the relatively high cost of the equipment.

An innovative non-contact method is the use of the laser generation – laser receiving technique. It consists in producing ultrasonic waves in both thermo-elastic and ablation regimes by using a pulsed laser beam striking the surface of the component to be inspected. A laser interferometer allows the detection of the ultrasonic waves on the surface after their interaction with the bulk

material and the defects eventually embedded within it [23]. Choi and Jhang [24] validated a finite element model of laser generated ultrasonic waves in ablation regime by creating internal artificial defects in a steel specimen and then comparing experimental results with the numerical ones. As far as the authors are aware, few research papers deal with the application of this technique in the railway fields, and they are especially focused on rails defects detection [25–28].

Generally, it is required to inspect all the wheels of a train which means several non-destructive investigations. Thus, for optimizing the out-of-service time of the train, it is a great challenge to develop a non-destructive method that allows flaws detection without disassembling the wheelset axles.

The difference between the present research and published ones [17] is the use of a laser interferometer to receive the ultrasonic waves instead of an air-coupled ultrasonic probe. Moreover, the receiving system allows the choice of the distance between the specimen and the interferometer by changing the focusing lens. This overcomes any encumbrance issue due to the equipment size. This aspect is an important advantage, considering that in air-coupled probes, the position and angle of the probe are generally fixed. In addition, in service conditions the tread of the wheel is very reflective (due to the contact with the rail) and this facilitates the reception of the ultrasonic waves by the interferometer. Even though the power level is set to generate UT in the ablation regime, the latter is barely reached since a line focalization was used, thus reducing the power density. Moreover, for B-scan maps generation, only one shot was recorded without any need for multiple shots (no averaging). Taking into account these aspects, the surface damage can be considered negligible.

Thus, the main novelty of this research is the application of the non-contact laser-laser ultrasonic technique on a train wheel, in which artificial defects were created to simulate real defects coming from operative conditions. Radial, axial defects and open-surface cracks with different widths were created on a rail wheel used by the Italian railway company Trenitalia SpA; the material and the geometry of the wheel are the same which can be encountered in the field. The main aim of the

research is to verify the potentialities and the applicability of the technique in the railway field and to verify its reliability on well-known defects.

2. Sample and experimental setup

To test the proposed diagnostic approach, a sector of a train wheel provided by Trenitalia SpA was used as benchmark. The wheel sample presents a set of six standard reproduced defects, indicated with the capital letters A to F. The geometries and positions of the defects are shown in Figure 1. Location and dimension of the artificial defects are in line with the most likely ones encountered on the worksite inspection. In Figure 2 a picture of the train wheel sector with some magnifications on the defected zone is reported.

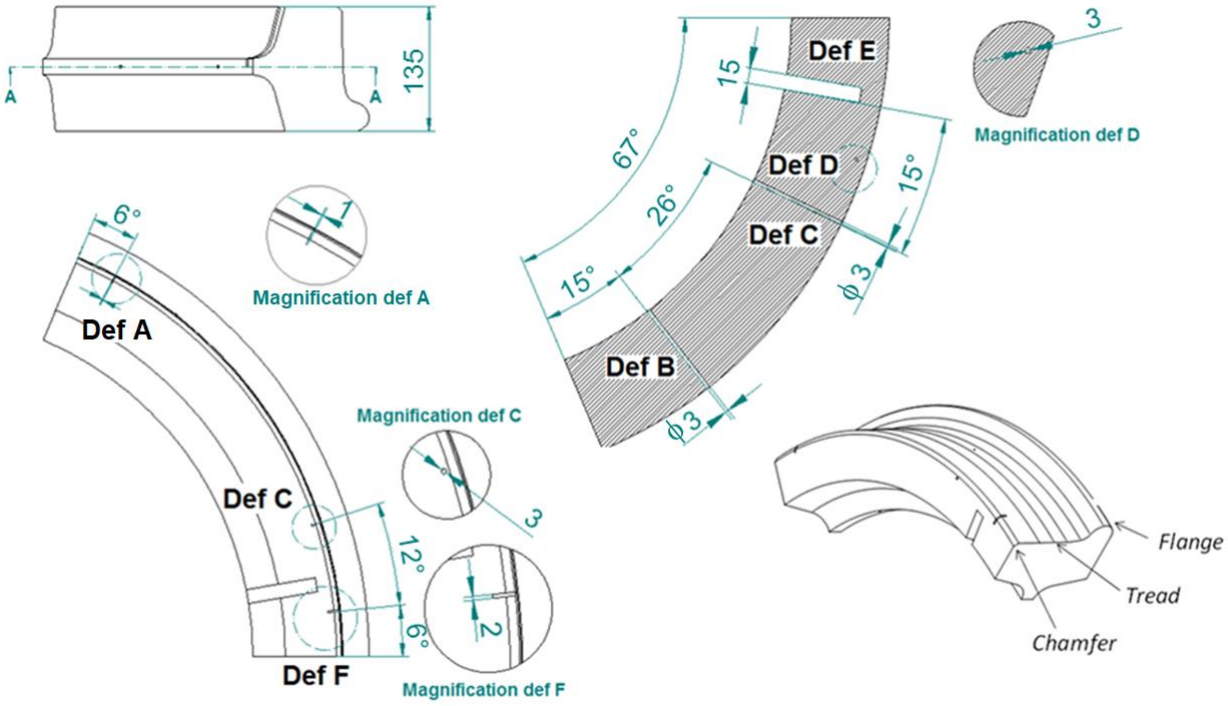

Figure 1 – Draft of the train wheel sector with dimensions and positions of the reproduced standard defects.

The experimental setup is composed of a pulsed laser for the Ultrasonic (UT) generation and a continuous wave (CW) laser as a UT receiver (see Figure 3). The laser transmitter is an IR Nd:YAG with wavelength of *1064 nm*, pulse duration of *8.5 nm* able to generates UT waves in the range between *1 MHz* and *50 MHz*, max frequency of multiple shooting *20 Hz*, *100 mJ* of energy; the

beam diameter, before any focusing lens, is equal to *4 mm*. The receiving unit combines a continuous-wave laser and an interferometer in order to acquire the surface out-of-plane displacements. The interferometer unit, which allows the detection of UT signal in the bandwidth up to *50 MHz*, has a wavelength of *532 nm* and a laser spot diameter of *~0.2 mm*.

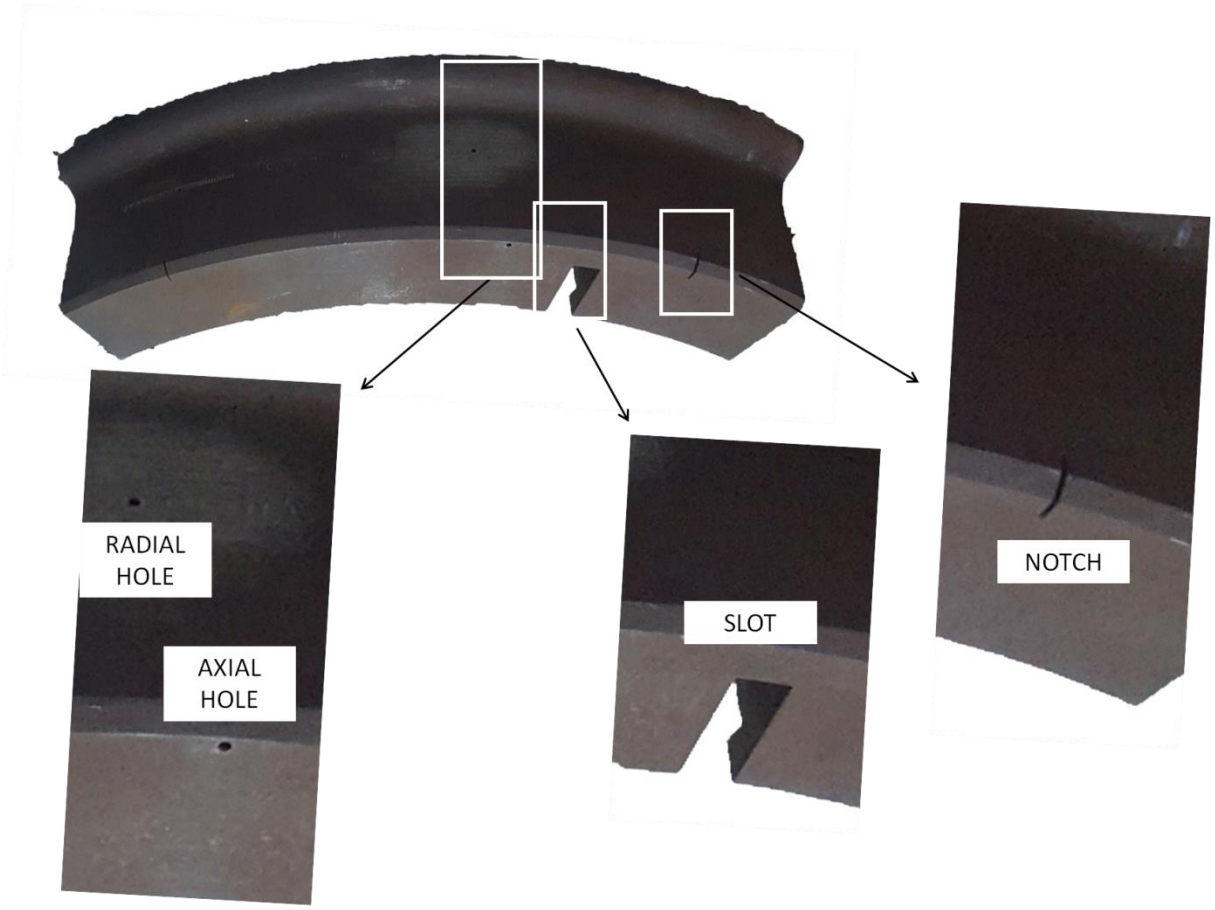

Figure 2 - Picture of the train wheel sector with magnification of the type of defects investigated.

The output signals from the interferometric unit are digitalized by an analogical to digital converter, triggered by the pulsed laser, and transferred to a PC for the generation of the B-scan. To perform the scan, the sample is moved by means of a motorized linear positioning system, triggered step by step from the acquisition and processing software installed on the PC.

Lasers source and receiver, with relative optics, are mounted on the optical bench, the distance between the specimen and the generation/receiving lasers can be chosen according with the focusing lenses employed, overcoming any encumbrance issues due to the equipment size. The

sample rotates synchronously around its centre; this condition was fundamental to maintain the focus of both laser beams over the sample surface during the rotation. The generation laser is focused in a line over the sample surface by adopting a cylindrical lens, reducing the power density injected in the sample surface and avoiding surface degradation; this kind of focalization favours the UT propagation over the direction normal to the focus line, optimizing the scan. The length of the focused line is about *3 mm* in order to be comparable with the defect dimensions. The laser interferometer was focused over the sample surface as a circle adopting spherical lens and at a distance from the generation laser line of *10 mm.* The sample is able to rotate by means of pulleys and a steel strand which transform the linear motion of the positioning system to a rotation (see Figure 3a). A picture of the UT setup is shown in Figure 3b.

To simulate a realistic in-service inspection setup, the generation and receiving devices are located on the same side in respect to the wheel tread, thus adopting the pitch-catch configuration. Wideband ultrasonic waves are generated with nanosecond laser pulses by setting the laser source in ablation regime in order to enhance the signal-to-noise ratio. However, the power level adopted in the generation of the UT signal was barely in the ablation regime because a line focalization was adopted instead of a pointwise one, hence reducing the power density. Moreover, to generate the B-scan maps only one shot for acquisition was needed without a need for multiple shots (no averaging). Taking into account these factors, the surface damage of the wheel can be considered negligible. The laser pulse generates longitudinal (L_W), shear, and surface (S_W) waves into the sample. A study on the UT angular propagation in the laser regimes can be found in [29].

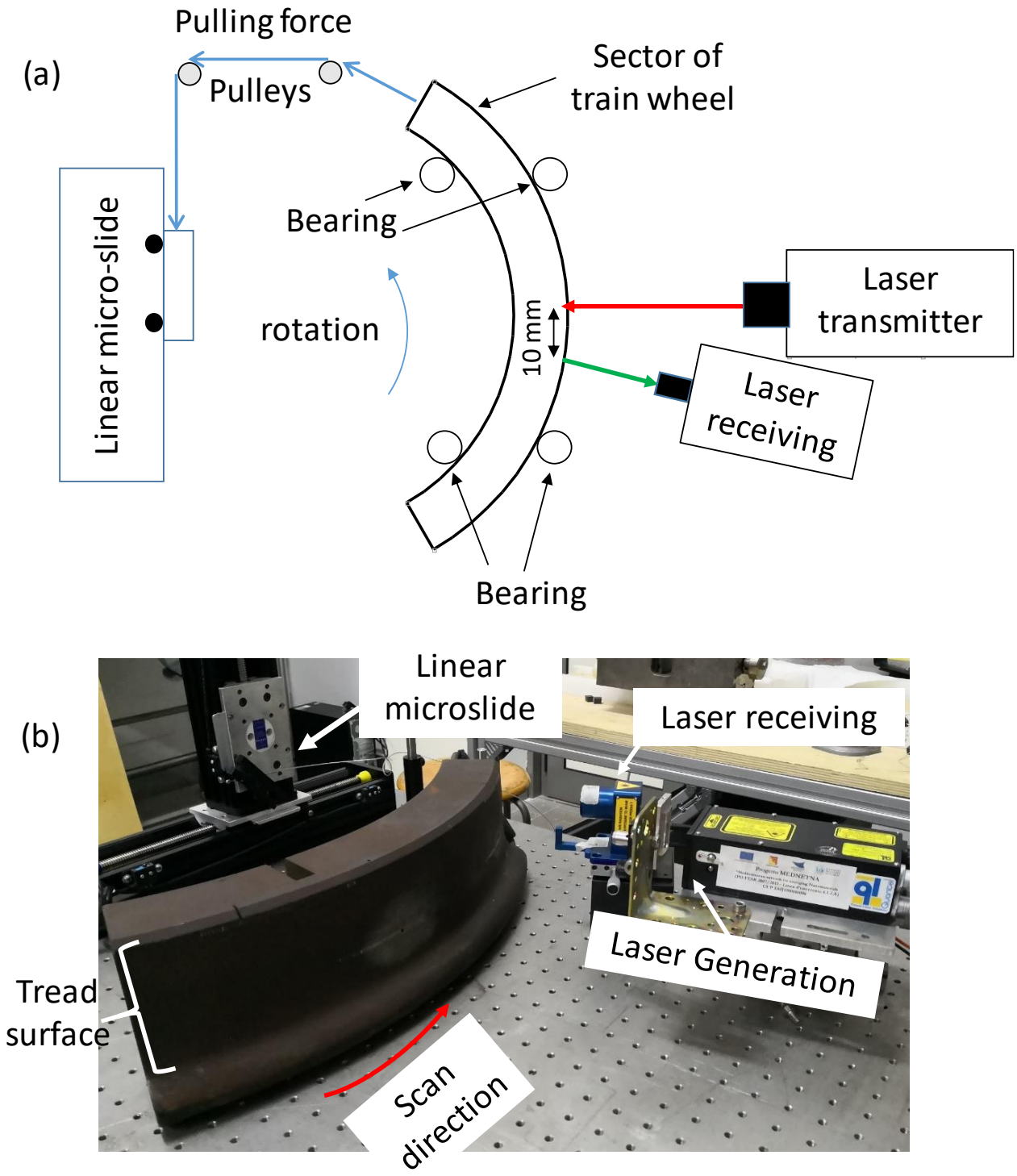

155

Figure 3 – Schematic representation of the experimental setup (a); picture of the laboratory setup (b).

In Figure 4a the detection mechanism for a superficial defect, such as A, B, C and F, is shown. The defect detection is based on the monitoring of the reflected surface wave (RS_W), which propagates

around the surface of the sample and is reflected by the defect edge. In Figures 4a and 4b the iS_W and iL_W are indicating the incident superficial and longitudinal waves respectively.

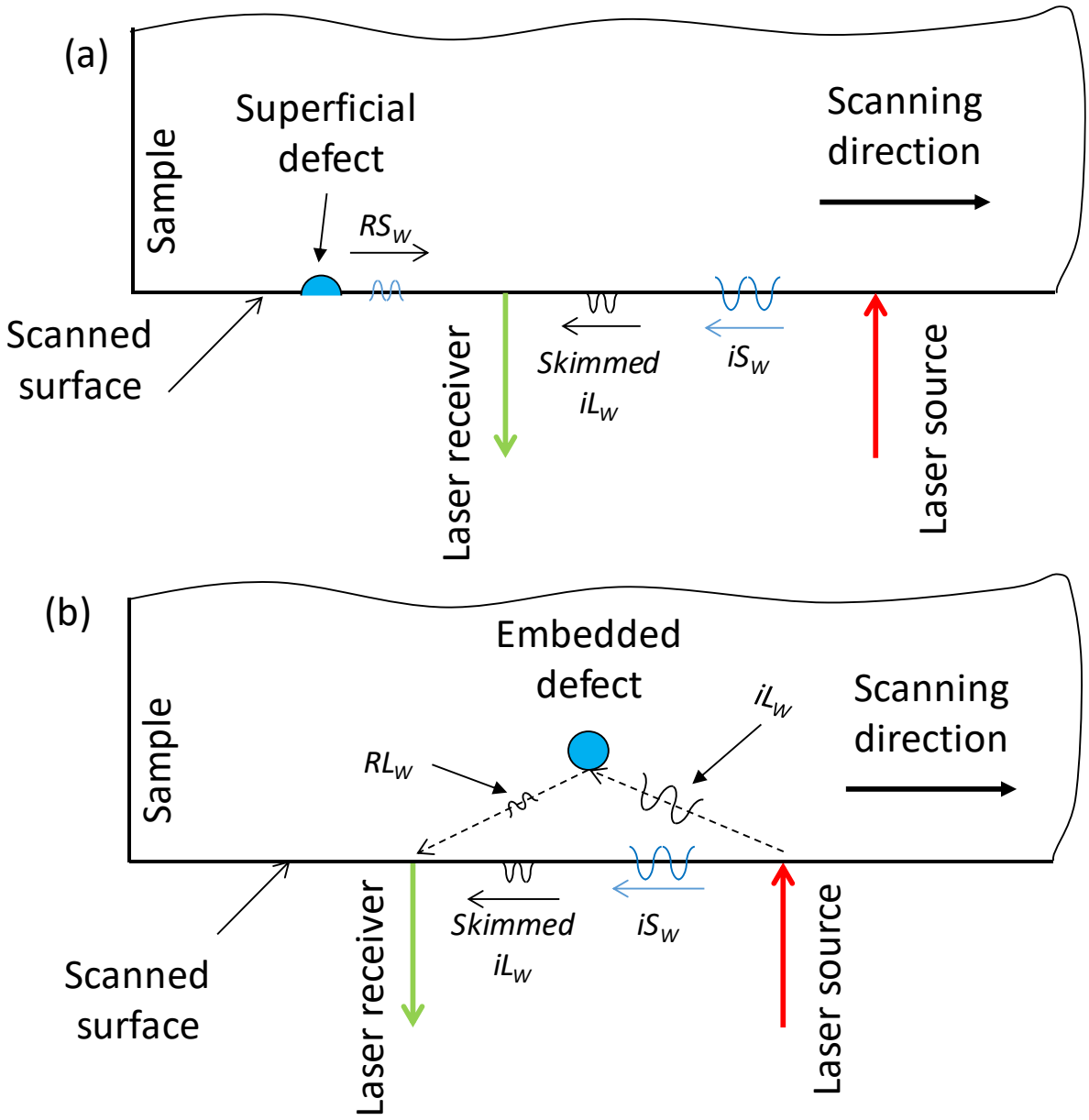

Figure 4 – Schematic 2D representation of the wave paths across the section of the sample for superficial (a) and embedded (b) defect evaluation.

In Figure 4b the detection mechanism adopted for the embedded defects, such as D and E, is shown. Since the defect is embedded the detection occurs by means of the reflected longitudinal wave RL_W propagating inside the material.

3. Results

The B-scan maps of the defected areas are shown and commented in this section. The wheel is moved in steps of *~2 mm* for each acquisition: this is the finer step possible with this setup. All the A-scan signals were stacked up and plotted in the B-scan maps. The abscissa and ordinate indicate the time and the laser position respectively. In the B-scan, the signal amplitudes were represented in the maps by a colour based scale.

In order to cut-off other reflected waves and enhance defect detection in the maps, the acquisition time-window has been optimized to include only the waves corresponding to defects (10 μs). No interpolation of the A-scan signals was needed in the generation of the B-scan maps because of the small distance between consecutive shots.

The inspection of the train wheel was focused on four defective areas relative to the Defect A, Defect B, Defect C and D and Defect E and F. Following, the results for each scan are shown.

Defect A - Notch on the chamfer (1 mm x 3 mm)

In Figure 5a the map of the defected A zone is presented. A perturbation on the B-scan due to the superficial defect can be easily spotted. As in the case of the UT waves diffracted by the crack tip [30,31], a change in the time of arrival of the diffracted ultrasound pulse (as the scan approaches the defect) forms a characteristic feature. The position of the defect can be clearly identified by the interruption of the iL_W and iS_W bands on the map. In fact, during the scan sweep there is a time when the laser receiver crosses the defect whose interposition acts as a barrier between the L_W and S_W waves and the receiver. The interruption of the L_W and of the S_W waves is a direct probe of the defect position on the sample surface (see Figure 5a).

For superficial defects, the length of the signal interruption (L_W and S_W) is equal to the sum of the distance between source and receiver (*10 mm*) and the defect extension. In this case, the extension of the defect (*1 mm*) is too fine as compared with the step (*2 mm*), and the observed interruption of

the signal is equal to the source - receiver distance (*10 mm)*. To obtain a more accurate defect extension, a finer step would be required.

In Figure 5b and 5c two normalized A-scan waves acquired on sound and defective zones, respectively, are shown. In both graphs the incident longitudinal and superficial waves can be seen, and their time-of-flight is in agreement with each wave velocity and the source - receiver distance. The A-scan of Figure 5c, acquired at a distance of *36 mm* (see ordinate of map 5a), clearly indicates the presence of a defect when looking at the reflected superficial wave RS_W.

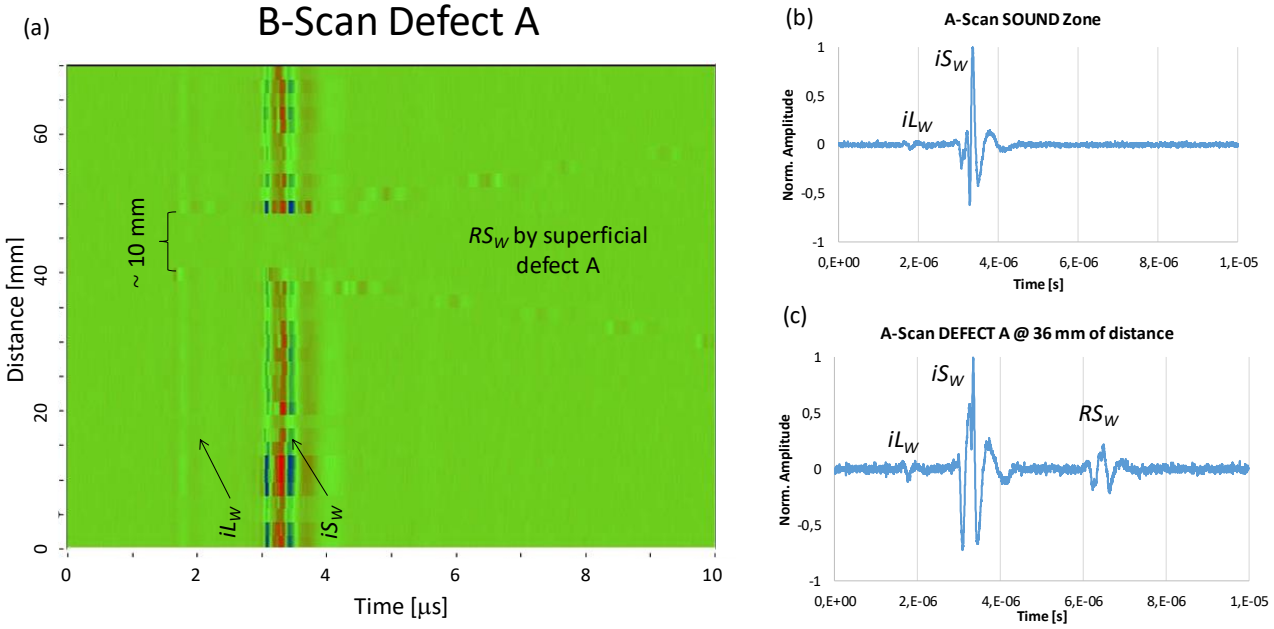

Figure 5 – B-Scan image of the scanned area near the superficial defect A (a); particular of the A-scan signals acquired on sound zone (b) and on the defected zone (c).

Defect B - Radial through hole

In Figure 6a the B-scan of defect B zones is presented. Similarly to superficial defect A, the position of the defect can be clearly spotted by the interruption of the iL_W and the iS_W bands due to the interposition of the defect between source and receiver. Thus, the result indicates that the defect B lies on the sample surface (see Figure 4a). The observed length of the interruption is *~12 mm*,

thus, subtracting the source – receiver distance (*10 mm*), the detected extension of the defects is *~2 mm*. In order to increase accuracy a finer step would be required.

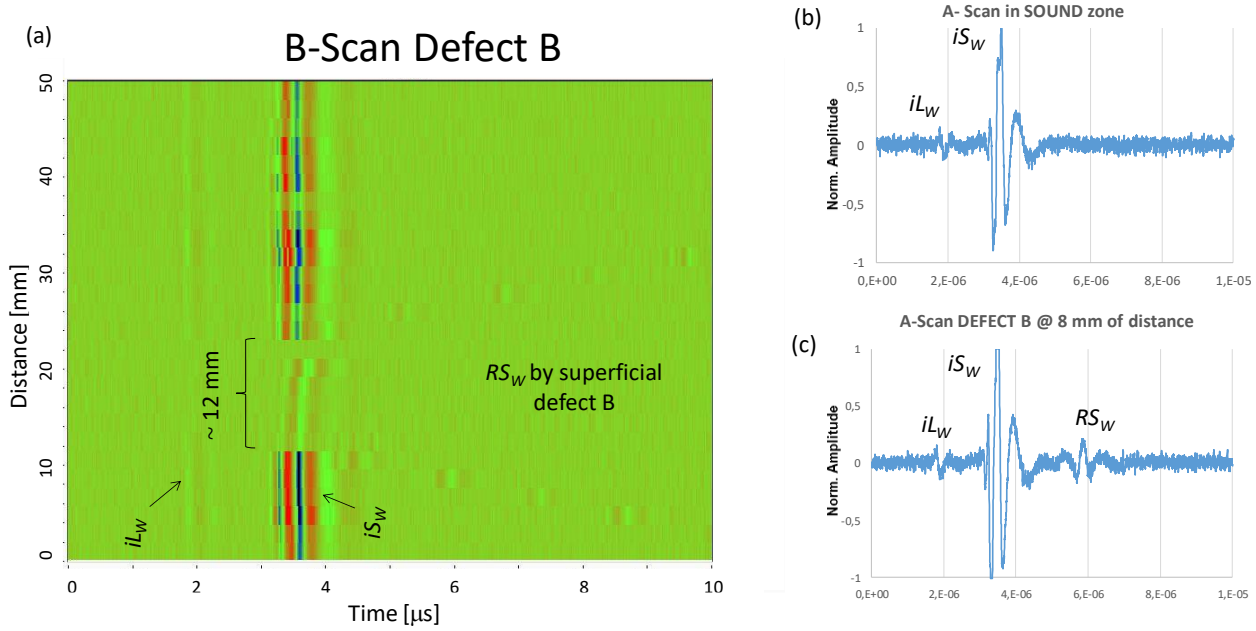

Figure 6 – B-Scan image of the scanned area near the superficial defect B (a); particular of the A-scan signals acquired on sound zone (b) and on the defected zone (c).

Here as well, in the A-scan graphs (see Figure 6b and 6c) the time-of-flight of the longitudinal iL_W and superficial iS_W waves is in agreement with the source - receiver distance and each wave velocity. In Figure 6c the reflected surface wave RS_W relative to the scan acquired at *8 mm* of distance can be clearly identified.

Defects C and D - Radial through hole and axial blind hole

In Figure 7a the B-scan for the area near defects C and D is shown. The perturbation induced by the superficial defect C can be explained as what already seen for the superficial defects A and B. The superficial position of defect C is clearly identified by the iL_W and iS_W interruption. Observing the length of the interruption (*~12 mm*) is then possible to estimate a *~2 mm* extension of the defect. Still, a finer step would help in increasing the extension accuracy.

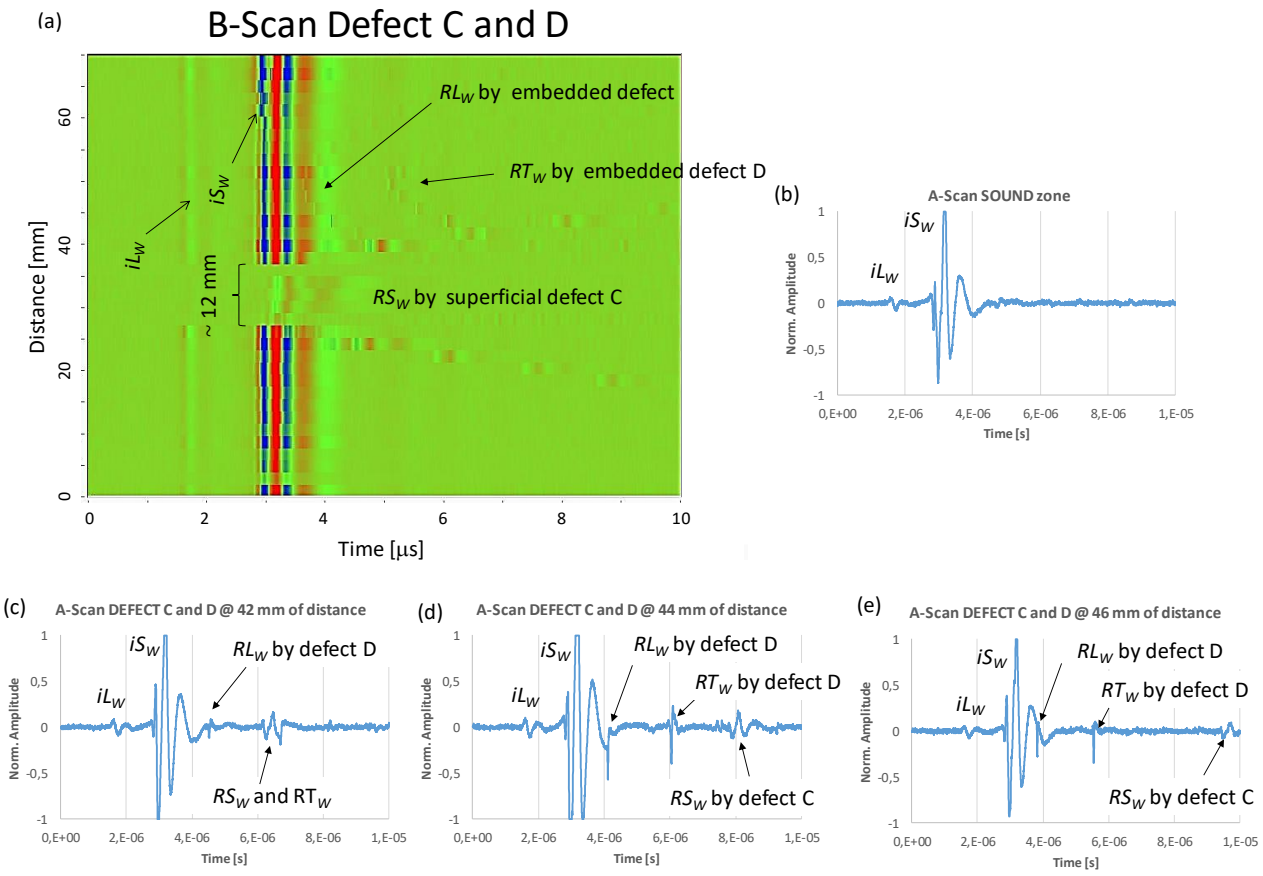

Figure 7 – B-Scan image of the scanned area near the superficial defect C and the embedded defect D (a); particular of the A-scan signals acquired on sound zone (b) and on the defected zones at different scan distances: in (c) *42 mm*, in (d) *44 mm*, in (e) *46 mm*.

Looking at Figure 7a, a peculiar parabolic signature generated by the inner defect D can be observed. A first parabolic pattern is generated by the longitudinal wave reflected by the defect edge (see RL_W in Figure 4b), a second shifted parabola is then formed by the reflected transversal wave (RT_W) generated at the defect edge. This latter parabola is in fact delayed because of the slower speed of the transversal wave in the medium. The vertex of the first parabola is found superimposed on the tail of the iS_W while the delayed second parabola does not interfere with the iL_W and iS_W signals. The plot of Figure 7e, acquired at *46 mm* of distance (almost in the vertex location), further proves this point by showing the RL_W superimposed on the tail of the iS_W. On the

same plot notice the reflected transversal wave RT_W relative to the delayed parabola and the reflected superficial wave RS_W (from the defect C) which is exiting the observation window. Going through the steps in reverse order, starting with the plot of Figure 7d *@ 44 mm*, the RT_W is slightly shifted on the left while the RS_W is greatly shifted on the same side with respect to the plot in Figure 7e. On the same graph the RL_W is now out of the tail of the iS_W. Continuing backwards to the plot of Figure 7c acquired *@ 42 mm*, the RT_W and RS_W are now superimposed generating a composed signal. In the plot of Figure 7b the A-scan signal acquired in the sound zone is reported.

It is worth noting that the temporal position of the parabolas of Figure 7a will depend on the source - receiver distance and on the defect depth, in fact, at fixed source - receiver distance, a more pronounced time shift indicates a deeper defect. The depth of the embedded defect D can be estimated using the time coordinate of the parabola vertex (of about *3.8 μs*); considering that the velocity of the longitudinal wave in steel is *5.85 mm/μs*, the travelled distance of the longitudinal wave is known $d = v_l \times t$ and is equal to *iLw* + *RLw* (see Figure 4b where an embedded defect is represented). Since a triangle can be constructed by using: *iLw* path, *RLw* path and source-receiver distance (see Figure 4b), the depth of the defect can be calculated as the height of said triangle (Pitagora's theorem). The calculated depth is here equal to *~10 mm*, and considering that the scan was performed in the middle of the sloped tread (with 10 % of slope) the results are in agreement with the data provided by Trenitalia SpA (see Figure 1). Further information about defect reconstruction adopting the time of flight diffraction can be found on [32].

Defects E and F - Slot on back side and notch on the chamfer (2 mm x 4 mm)

In Figure 8a the B-scan of defected E and F zones is presented. The perturbation induced by the superficial notch F can be explained in much the same way as already done for the superficial defects. Still here the position of the superficial defect F can be identified by the interruption of the iL_W and the iS_W bands. The estimated extension leads to a very small extension of the defect of *~1 mm*.

Due to its rectangular shape, the Defect E shows a relatively large face almost parallel to the scanned surface (see Figure 1 and 2). For this reason, defect E behaves like a back-wall thus, in the map of Figure 8a, it shows as a segment-like shape, with its extension equal to that of the defect (*15 mm*). Even here the depth of the defect can be easily evaluated by using trigonometric formula and is equal to *~20 mm*, in agreement with what is reported in the draft provided by Trenitalia SpA (see Figure 1).

As always, the iL_W and iS_W waves of the A-scan normalized signal of Figure 8b, 8c and 8d are in agreement with the time-of-flight relative to the source - receiver distance. On the plot of Figure 8c it is possible to see the RL_W signal relative to the defect F, while in Figure 8d the RS_W signal relative to the superficial defect E.

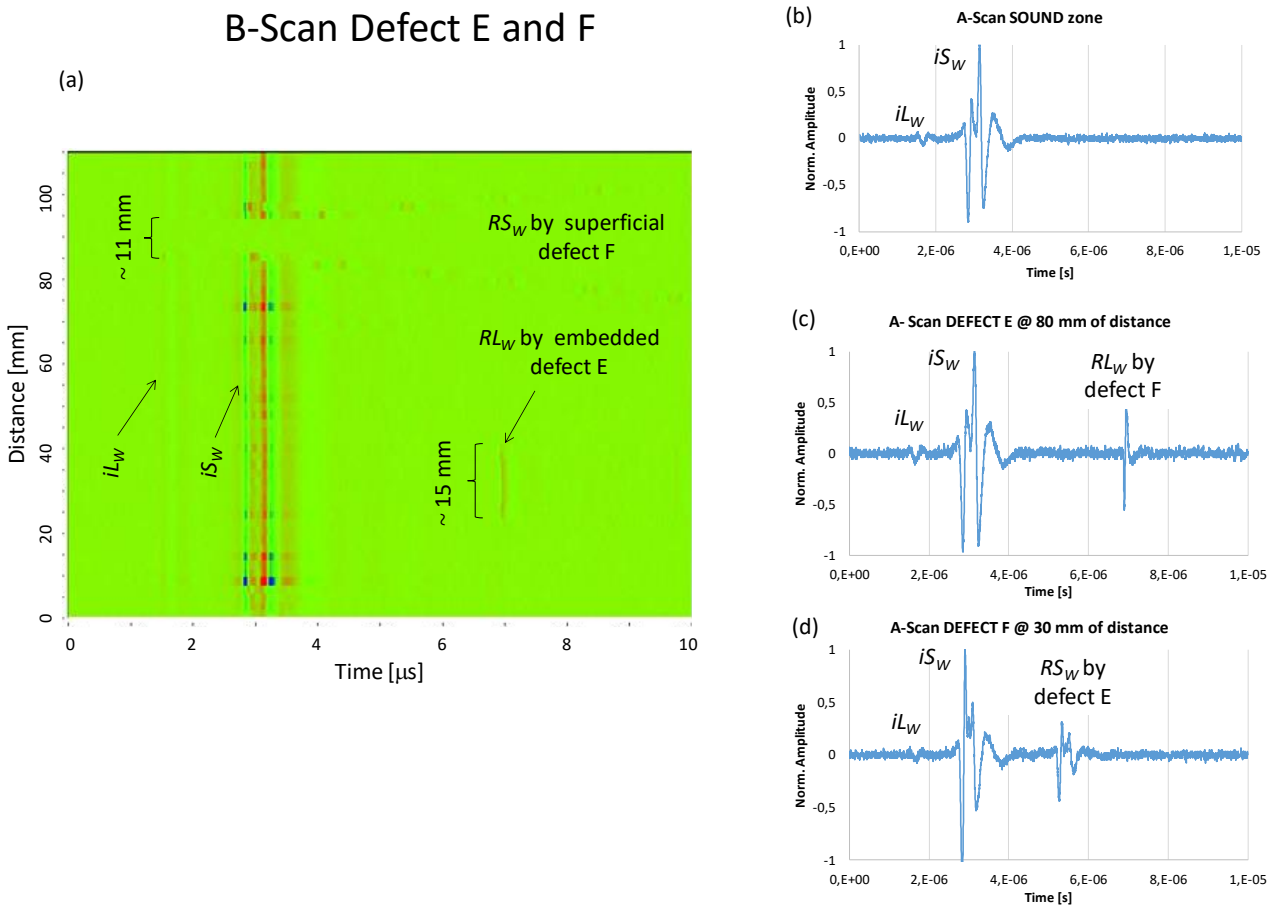

Figure 8 – B-Scan image of the scanned area near the embedded defect E and superficial defect F (a); particular of the A-scan signals acquired on sound zone (b) on the defected zone E (c) and on the defected zone F (d).

4. Conclusions

In this work, the applicability of a non-contact laser based ultrasonic technique has been proven for the detection of defects in a train wheel. The proposed technique uses a pulsed IR Nd:YAG laser for the wideband ultrasonic generation and a continuous wave laser interferometer for the ultrasonic reception. A set of standard defects, in accordance with likely ones encountered in worksite inspection, have been artificially created in a rail wheel, provided by the Italian railway company Trenitalia SpA.

The proposed setup, when compared with the more conventional approaches, has the main advantage of being non-contact and remote, allowing to avoid coupling media, enhancing the robustness of the results and overcoming the adaptability and accessibility issues. The main cons regard nowadays cost of the equipment.

The laser based approach was able to locate all the typology of standard wheel defects whether they are superficial or embedded, however more efforts are still needed for accurate defect reconstruction. A possible way to inspect the wheels on the field is to mount the equipment on a trail moving parallel to the wagon, focusing both lasers on each wheel, one at a time. The scan can be executed without disassembling the wheelset axles and, even if the active scanning time is longer, time can be saved by avoiding out of service and disassembly.

In the light of obtained results, the application of this technique for in-service inspection of train wheels and other rail components is considered quite promising.

Acknowledgements

The authors would like to thank Trenitalia SpA, “Direzione Tecnica Ingegneria Rotabili e Tecnologie di Base, Tecnologie Meccaniche e Sistemi Frenanti, Processi Speciali” and “Unità Operativa CND” and mainly Luca Labbadia, Valentina Leonardi and Marco Sarti for their support and for providing the train wheel.

References

[1] Peng D, Jones R, Constable T, Lingamanaik SN, Chen BK. The tool for assessing the damage tolerance of railway wheel under service conditions. Theor Appl Fract Mech 2012;57:1–13. doi:10.1016/j.tafmec.2011.12.002.

[2] Ekberg A, Åkesson B, Kabo E. Wheel/rail rolling contact fatigue - Probe, predict, prevent. Wear 2014;314:2–12. doi:10.1016/j.wear.2013.12.004.

[3] Hannemann R, Köster P, Sander M. Fatigue crack growth in wheelset axles under bending and torsional loading. Int J Fatigue 2019;118:262–70. doi:10.1016/j.ijfatigue.2018.07.038.

[4] Le M, Jun J, Kim J, Lee J. Nondestructive testing of train wheels using differential-type integrated Hall sensor matrixes embedded in train rails. NDT E Int 2013;55:28–35. doi:10.1016/j.ndteint.2013.01.003.

[5] Crupi V, Epasto G, Guglielmino E, Risitano G. Analysis of temperature and fracture surface of AISI4140 steel in very high cycle fatigue regime. Theor Appl Fract Mech 2015;80:22–30. doi:10.1016/j.tafmec.2015.07.007.

[6] Naeimi M, Li Z, Qian Z, Zhou Y, Wu J, Petrov RH, et al. Reconstruction of the rolling contact fatigue cracks in rails using X-ray computed tomography. NDT E Int 2017;92:199–212. doi:10.1016/j.ndteint.2017.09.004.

[7] Zhou L, Brunskill HP, Lewis R. Real-time non-invasive measurement and monitoring of wheel–rail contact using ultrasonic reflectometry. Struct Heal Monit 2019:1–13. doi:10.1177/1475921719829882.

[8] Cavuto A, Martarelli M, Pandarese G, Revel GM, Tomasini EP. Experimental investigation by laser ultrasonics for high speed train axle diagnostics. Ultrasonics 2015;55:48–57. doi:10.1016/j.ultras.2014.08.010.

[9] Mineo C, Cerniglia D, Pantano A. Numerical study for a new methodology of flaws detection in train axles. Ultrasonics 2014;54:841–9. doi:10.1016/j.ultras.2013.10.008.

[10] Kappes W, Hentschel D, Oelschlägel T. Potential improvements of the presently applied in-service inspection of wheelset axles. Int J Fatigue 2016;86:64–76. doi:10.1016/j.ijfatigue.2015.08.014.

[11] Filograno ML, Corredera P, Rodríguez-Plaza M, Andrés-Alguacil A, González-Herráez M. Wheel flat detection in high-speed railway systems using fiber bragg gratings. IEEE Sens J 2013;13:4808–16. doi:10.1109/JSEN.2013.2274008.

[12] Stratman B, Liu Y, Mahadevan S. Structural health monitoring of railroad wheels using wheel impact load detectors. J Fail Anal Prev 2007;7:218–25. doi:10.1007/s11668-007-9043-3.

[13] Verkhoglyad AG, Kuropyatnik IN, Bazovkin VM, Kuryshev GL. Infrared diagnostics of cracks in railway carriage wheels. Russ J Nondestruct Test 2009;44:664–8. doi:10.1134/s1061830908100021.

[14] Alemi A, Corman F, Lodewijks G. Condition monitoring approaches for the detection of railway wheel defects. Proc Inst Mech Eng Part F J Rail Rapid Transit 2017;231:961–81. doi:10.1177/0954409716656218.

[15] Kenderian S, Cerniglia D, Djordjevic BB, Green RE. Laser-generated acoustic signal interaction with surface flaws on rail wheels. Res Nondestruct Eval 2005;16:195–207. doi:10.1080/09349840500306006.

[16] Pohl R, Erhard A, Montag HJ, Thomas HM, Wüstenberg H. NDT techniques for railroad wheel and gauge corner inspection. NDT E Int 2004;37:89–94. doi:10.1016/j.ndteint.2003.06.001.

[17] Cavuto A, Martarelli M, Pandarese G, Revel GM, Tomasini EP. Train wheel diagnostics by laser ultrasonics. Meas J Int Meas Confed 2016;80:99–107. doi:10.1016/j.measurement.2015.11.014.

[18] Zerbst U, Mädler K, Hintze H. Fracture mechanics in railway applications - An overview. Eng Fract Mech 2005;72:163–94. doi:10.1016/j.engfracmech.2003.11.010.

[19] Salzburger HJ, Schuppmann M, Wang L, Gao X. In-motion ultrasonic testing of the tread of high-speed railway wheels using the inspection system AUROPA III. Insight Non-Destructive Test Cond Monit 2009;51:370–2. doi:10.1784/insi.2009.51.7.370.

[20] Peng J, Wang L, Zhang Y, Gao X, Wang Z, Zhao Q, et al. The Design and Application of Lateral Phased Array Probe for Railway Wheel Rim Ultrasonic Detection System. 18th WCNDT, South Africa., 2012, p. 16–20.

[21] Kenderian S, Djordjevic BB, Cerniglia D, Garcia G. Dynamic railroad inspection using the laser-air hybrid ultrasonic technique. Insight - Non-Destructive Test Cond Monit 2006;48:336–41. doi:10.1784/insi.2006.48.6.336.

[22] Cerniglia D, Montinaro N, Nigrelli V. Detection of disbonds in multi-layer structures by laser-based ultrasonic technique. J Adhes 2008;84:811–29. doi:10.1080/00218460802443295.

[23] Yamamoto S, Hoshi T, Miura T, Semboshi J, Ochiai M, Fujita Y, et al. Defect Detection in Thick Weld Structure Using Welding In-Process Laser Ultrasonic Testing System. Mater Trans 2014;55:998–1002. doi:10.2320/matertrans.i-m2014809.

[24] Choi S, Jhang KY. Internal defect detection using laser-generated longitudinal waves in ablation regime. J Mech Sci Technol 2018;32:4191–200. doi:10.1007/s12206-018-0817-1.

[25] Yunjie Z, Xiaorong G, Lin L, Yongdong P, Chunrong Q. Simulation of Laser Ultrasonics for Detection of Surface-Connected Rail Defects. J Nondestruct Eval 2017;36:1–10. doi:10.1007/s10921-017-0451-3.

[26] Jiang Y, Wang H, Tian G, Yi Q, Zhao J, Zhen K. Fast classification for rail defect depths using a hybrid intelligent method. Optik (Stuttg) 2019;180:455–68. doi:10.1016/j.ijleo.2018.11.053.

[27] Kenderian S, Cerniglia D, Djordjevic BB, Garcia G, Sun J, Snell M. Rail track field testing using laser/air hybrid ultrasonic technique. Mater Eval 2003;61.

[28] Kenderian S, Cerniglia D, Djordjevic BB, Garcia G. Laser-air hybrid ultrasonic technique for dynamic railroad inspection applications. Insight Non-Destructive Test Cond Monit 2005;47:336–40. doi:10.1784/insi.47.6.336.66454.

[29] C.B Scruby L. D. Laser Ultrasonics Techniques and Applications. CRC Press; 1990.

[30] Petcher PA, Dixon S. A modified Hough transform for removal of direct and reflected surface waves from B-scans. NDT E Int 2011;44:139–44. doi:10.1016/j.ndteint.2010.11.004.

[31] Petcher PA, Dixon S. Parabola detection using matched filtering for ultrasound B-scans. Ultrasonics 2012;52:138–44. doi:10.1016/j.ultras.2011.07.006.

[32] Scafidi M, Cerniglia D, Ingrassia T. 2D size, position and shape definition of defects by B-

scan image analysis. Frat Ed Integrita Strutt 2015;9:622–9. doi:10.3221/IGF-ESIS.34.68.

400